RESEARCH ARTICLE

Key Points:
- We present the first maps of the absorption of auroral FUV emission by methane
- The penetration depth of auroral electrons layer is highly spatially variable
- The electron energy reaches as much as 500 keV in the polar region

Correspondence to:
J.-C. Gérard,
jc.gerard@ulg.ac.be

Mapping the electron energy in Jupiter's aurora: Hubble spectral observations

J.-C. Gérard[1], B. Bonfond[1], D. Grodent[1], A. Radioti[1], J. T. Clarke[2], G. R. Gladstone[3], J. H. Waite[3], D. Bisikalo[4], and V. I. Shematovich[4]

[1]LPAP, Université de Liège, Liège, Belgium, [2]CSP, Boston University, Boston, Massachusetts, USA, [3]SwRI, San Antonio, Texas, USA, [4]INASAN, Russian Academy of Sciences, Moscow, Russia

Abstract Far ultraviolet spectral observations have been made with the Hubble Space Telescope in the time-tag mode using the Space Telescope Imaging Spectrograph (STIS) long slit. The telescope was slewed in such a way that the slit projection scanned from above the polar limb down to midlatitudes, allowing us to build up the first spectral maps of the FUV Jovian aurora. The shorter wavelengths are partly absorbed by the methane layer overlying part of the auroral emission layer. The long-wavelength intensity directly reflects the precipitated energy flux carried by the auroral electrons. Maps of the intensity ratio of the two spectral regions have been obtained by combining spectral emissions in two wavelength ranges. They show that the amount of absorption by methane varies significantly between the different components of the aurora and inside the main emission region. Some of the polar emissions are associated with the hardest precipitation, although the auroral regions of strong electron precipitation do not necessarily coincide with the highest electron energies. Outputs from an electron transport model are used to create maps of the distribution of the characteristic electron energies. Using model atmospheres adapted to auroral conditions, we conclude that electron energies range between a few tens to several hundred keV. Comparisons of derived energies are in general agreement with those calculated from magnetosphere-ionosphere coupling models, with values locally exceeding the standard model predictions. These results will provide useful input for three-dimensional modeling of the distribution of particle heat sources into the high-latitude Jovian upper atmosphere.

1. Introduction

The first detection of Jupiter's far ultraviolet (FUV) aurora was based on spectra collected with the Ultraviolet Spectrometer during the flybys of the Voyagers 1 and 2 spacecraft in 1980. They showed the presence of a ring of HI Lyman α and H_2 Lyman and Werner bands emission in the polar regions of both hemispheres [*Broadfoot et al.*, 1981]. The Faint Object Camera on board the Hubble Space Telescope (HST) provided the first FUV images of the northern Jovian aurora [*Gérard et al.*, 1993; *Clarke et al.*, 1996]. With the improved sensitivity of the successive generations of cameras on board HST (Wide-Field Planetary Camera 2 (WFPC2), Space Telescope Imaging Spectrograph (STIS), and Advanced Camera for Surveys (ACS)), further morphological features and characteristics were discovered, so that today an extensive database of auroral images is available and our knowledge of the magnetosphere-ionosphere coupling has remarkably improved. The morphological characteristics of Jupiter's aurora have been reviewed by various authors [*Bhardwaj and Gladstone*, 2000; *Mauk et al.*, 2002a; *Clarke et al.*, 2004; *Grodent*, 2014; *Badman et al.*, 2014]. Observations with the HST FUV cameras also made it possible to investigate the auroral response to the solar wind activity [*Clarke et al.*, 2009; *Nichols et al.*, 2009]. The energy powering the magnetospheric plasma finds its origin in the fast planetary rotation and its subsequent transfer into kinetic energy of magnetospheric electrons. Unlike the Earth's and Saturn's cases, conceptual models [*Hill*, 2001; *Cowley and Bunce*, 2001; *Cowley et al.*, 2003] suggest that the relatively stable main auroral emission at Jupiter corresponds to the upward branch of a global current system flowing along magnetic field lines. Other acceleration processes appear to be at play in other regions of the magnetosphere. For example, pitch angle scattering of energetic electrons is thought to be the source of the diffuse aurora observed equatorward of the main oval [*Radioti et al.*, 2009]. Polar regions inside the main emission show rapidly varying and flaring structures whose origin is still largely unknown [*Waite et al.*, 2001; *Grodent et al.*, 2003; *Bonfond et al.*, 2011]. Finally, the magnetic footprints of the Galilean satellite on the Jovian atmosphere [*Clarke et al.*, 2002] appear to be generated by a parallel electric field associated with the propagation of Alfvèn waves [*Jones and Su*, 2008; *Hess et al.*, 2013]. It is very likely that the characteristic electron energy associated with these various processes is different, but it is currently largely unknown.

Physical understanding of Jupiter's magnetosphere and acceleration mechanisms requires measurements of the energy distribution of precipitating particles producing the aurora. For example, images of Jupiter's FUV aurora show that the morning sector aurora is generally thinner and more stable than other parts of the oval [*Clarke et al.*, 2004], but it is not known whether the precipitated electron energy is harder there than in other regions. Such are currently inaccessible to in situ measurements on a global scale. Mapping the characteristic energy of auroral electrons is thus a major scientific breakthrough for two reasons: (i) auroral electron energy bears the signature of the energization processes whose identification is essential to understand the magnetosphere-ionosphere coupling of giant and extrasolar planets, and (ii) auroral precipitation on Jupiter provides a power over $1–5 \times 10^{13}$ W, a value exceeding by far the contribution of solar radiation input into the upper atmosphere, which deeply modifies the thermal and wind structure in the upper atmosphere.

The aurorae of giant planets potentially exert a major influence on the thermal structure and the chemistry of the planets' upper atmosphere. Auroral precipitation has important consequences for the vertical distribution of auroral heat input. Models have demonstrated that the solar EUV heat input alone is insufficient to heat the upper atmosphere to the observed ~1000 K [*Lam et al.*, 1997]. The effect of auroral precipitation on the thermal structure is strongly dependent on the energy of the auroral electrons and the altitude of deposition of heat by particle precipitation and Joule heating. Three-dimensional models of the thermospheric general circulation have investigated the role played by the aurora in the energy balance, transport by winds, thermal structure, and composition of the Jovian upper atmosphere [*Achilleos et al.*, 1998; *Bougher et al.*, 2005]. The atmospheric heat balance depends on the energy of the incoming particles and the partitioning of energy between particle and Joule heating, advection, UV emission, and cooling by infrared H_3^+ radiation and by hydrocarbon thermal emission.

Information on the energy of the precipitated auroral electrons can currently only be obtained through ultraviolet spectral remote sensing. In situ electron energy measurements must be made below the acceleration region to probe to the population causing the aurora. The depth of the aurora relative to the hydrocarbon homopause has been determined based on the comparison between observed spectra and a reference H_2 laboratory spectrum without any absorption. The methane column providing the best fit allows the determination of the location of the auroral emission peak relative to the hydrocarbon homopause, which is linked to the energy of the precipitating electrons. This method is based on the shape of the CH_4 absorption cross sections, which partly absorbs the H_2 emissions at wavelengths shorter than 140 nm but leaves the longer wavelength H_2 emissions unattenuated. Low-spectral resolution Voyager-ultraviolet spectrometer (UVS) spectra [*Broadfoot et al.*, 1981] showed signature of absorption by methane. Coupled with an electron transport model, the FUV color ratio [*Yung et al.*, 1982] has been used to determine the characteristic energy of the precipitation. These and subsequent spectra measured with the International Ultraviolet Explorer, the Hopkins Ultraviolet Telescope (HUT), and the UVS spectrometer on board the Galileo spacecraft [*Livengood et al.*, 1990; *Harris et al.*, 1996; *Morrissey et al.*, 1997; *Ajello et al.*, 1998] were not spatially resolved and were analyzed to determine spatially averaged color ratio (CR) defined here as

$$CR = I(155 - 162)/I(123 - 130), \tag{1}$$

where the nominator is the intensity (in photon units) integrated from 155 to 162 nm and the denominator is the total intensity between 123 and 130 nm. The value of the color ratio in the absence of any absorption is equal to 1.1.

Partial spatial resolution was first obtained with the Goddard High Resolution Spectrometer (GHRS) on board HST which intercepted a 2″ × 2″ sector on the planet [*Trafton et al.*, 1994; *Kim et al.*, 1997]. *Dols et al.* [2000] analyzed auroral GHRS spectra collected at different latitudes and local times. They found values of the methane slant column density in the range 2.3 to 70×10^{16} cm^{-2} and deduced variations of the mean electron energy between 35 and 80 keV. Spectra collected with the STIS long slit at 1.2 nm spectral resolution at different auroral locations were analyzed by *Gustin et al.* [2004a] and compared with synthetic or laboratory spectra of electron-excited H_2 UV emissions [*Gustin et al.*, 2006]. They derived characteristic energies in the range 30–200 keV, reaching as much as 400 keV in a bright morning event. *Gérard et al.* [2003] obtained time-tagged STIS spectra of the polar emission and showed that the overlying methane column densities varied over a few minutes. The corresponding mean energy of the primary auroral electrons ranged between 40 and 120 keV. The major source of uncertainties is linked to the vertical distribution of the absorbing hydrocarbons in the high-latitude regions.

Another approach was based on self-absorption of optically thick EUV H_2 bands. The comparison of the observed spectrum below about 110 nm with a laboratory or synthetic spectrum optically thin H_2 spectrum made it possible to estimate the depth of the auroral emission. This technique was first applied to auroral spectra obtained with the HUT instrument on board the Space Shuttle [*Wolven and Feldman*, 1998]. Later, EUV spectra of the global aurora showing signatures of self-absorption by H_2 were obtained with Far Ultraviolet Spectroscopic Explorer (FUSE) and analyzed by *Gustin et al.* [2004b]. They concluded that the energy distribution that best globally fitted three FUSE spectra was a sum of Maxwellian functions with characteristic energies ranging from 1 to 100 keV, giving rise to an emission peak located at 5 μbar, that is ~275 km above the 1 bar level.

The morning aurora generally appears brighter and more confined in latitude than the diffuse afternoon aurora [*Clarke et al.*, 2004], but new observations from different central meridian longitudes are required to resolve the longitude-local time ambiguity and constrain models of the acceleration processes. Additionally, it is useful to compare absorption maps of the north and south polar regions to search for possible systematic differences. The combination of the unique STIS spectral imaging capability with a spatial scan of the auroral region can provide spatially resolved measurements of the FUV absorption by methane that may be used to map the penetration of auroral electrons relative to the methane homopause. For the first time in this study, spatially resolved HST measurements of Jupiter's FUV spectrum and two-dimensional mapping of the amount of hydrocarbon absorption collected for the first time are described and analyzed.

The spectral scan observations are described in section 2, and the determination of the pixel coordinates and the image processing are presented in section 3. Section 4 presents the observed morphology of the brightness and color ratio distributions. The results of the comparison of the model simulations with the spectral observations are discussed in section 5 and compared with earlier determinations of the depth of the aurora and characteristic energy of the auroral electrons. Conclusions concerning the energy distribution in the Jovian aurora are summarized in section 6.

2. STIS Spectral Spatial Scans

The HST observations were collected near opposition in January and March 2014 in both hemispheres under different central meridian longitudes (CML). The STIS Multi-Anode Microchannel Array (MAMA) imaging spectrograph was operated in the long-slit spectral mode with the G140L grating. The effective aperture was 26×0.5 arc sec, providing a spectral resolution of ~1.2 nm. The STIS instrument, its observing modes and in-orbit performance were described by *Kimble et al.* [1998]. Time-tagged dayside auroral spectra were successfully obtained covering the wavelengths 115–170 nm.. The time-tag mode makes it possible to analyze the photon stream reaching the detector, to isolate regions on the planet during the postprocessing phase. The 0.5 arc sec aperture width corresponds to the field of view subtended by 20 pixels on the STIS MAMA detector, much broader than the STIS spatial resolution in the FUV imaging mode. When projected at Jupiter's distance from Earth on the planetary disk during the period of the observations, it corresponds to a perpendicular distance ranging between 1530 and 1760 km during the time of these observations, corresponding to ~1.3 degree of latitude at the equator.

On four occasions the Hubble Space Telescope performed maneuvers to move the slit projection across the polar regions while collecting FUV auroral spectra. The observations were divided into four visits of one orbit each, which took place on 8 and 15 January and 15 March 2014 in the north, and 14 January in the south. During the observations, the Space Telescope was slewed in such a way that the slit projection scanned the disk from above the polar limb down to midlatitudes. The spacecraft was rolled about its optical axis so that the STIS slit was inclined at a low angle relative to the planetary equator to best collect auroral photons and maximize the chances to intercept the strongest emission regions during the telescope slew.

Table 1 lists the dates, times and central longitudes of the four visits performed in the frame of HST program 13402. The spectral observations lasted approximately 42 min during each visit. During the January 14 visit, the telescope pointed slightly off target, so that part of the afternoon and evening main auroral emission was missed. This observation was repeated on March 15, under slightly different conditions (Table 1).

3. Image Processing

Starting from the time-tag event lists, our objective is to create pseudo images having the same pixel size along the slit and across the slit. Hence, we determine the amount of time required for HST to slew across the

Table 1. HST Spectral Scans of the Jovian FUV Aurora

Date (2014)	Hemisphere	Start UT	CML[a]	Earth-Jupiter Distance (AUs)
8 Jan	North	23:06	155°–188°	4.21
12 Jan	South	22:43	24°–48°	4.22
14 Jan	North	00:13	229°–253°	4.22
15 Mar	North	18:34	207°–231°	4.85

[a]Range of S_{III} longitudes during the STIS exposure.

angle subtended by the pixel size (0.024″). Using this time interval as the integration time for each frame, we built and calibrated a series of successive two-dimensional spectra. The brightness of the pixels corresponding to the appropriate spectral domain was summed in order to form a brightness vector along the long-slit direction. These successive vectors were then stacked along each other to form the required pseudo image. It is noticeable that each band perpendicular to the slit direction has been acquired at a different time and that the planet rotated by 25° between the first and the last lines. It should be noted that even though the pixel sizes in the x axis (along the slit) and in the y axis are equal, the pseudoimages appear smeared out across the slit because of the finite slit width. The positioning of the different components of the aurora on the planet requires one to identify the center of the planet in the pseudoimages. On FUV images obtained directly from HST cameras, this operation is usually performed through a limb-fitting procedure. This is possible since the observed Jovian disk is dominated by the "red leak," i.e., the residual sensitivity of the photocathode to near ultraviolet photons reflected by the planet [*Bonfond et al.*, 2009]. While these photons contaminate the imaging observations, they also create a crisp limb corresponding to the 1 bar level. By contrast, our spectral observations are not affected by the red leak, which prevents us from using this method. Instead, we used the location of the satellite footprints as landmarks. The Io footprint is present and easy to identify on three of the four images and so is the Ganymede footprint on the fourth one. The footprint y axis location corresponds to a specific time, and to this time corresponds a System III (S_{III}) longitude of Io. Using the Io footprint reference ovals from *Bonfond et al.* [2009] and *Hess et al.* [2011], we infer the longitude and the latitude of the footprint on the planet. Knowing the plate scale and the orientation of the slit relative to the Jovian rotation axis, we then computed the location of the planetary center relative to this footprint location. Due to smearing of the pseudoimages, we estimate that the uncertainty of the center location is on the order of half the slit width. Once the location of the center of Jupiter on the pseudoimage is known, a polar projection may be performed, bearing in mind that the central CML changes with time during the exposure. Thus, each image line must be projected independently according to the CML corresponding to the time of observation of this particular line, so that we map to true instantaneous S_{III} longitudes.

The local intensities of the total H_2 emission in the 125–180 nm window are estimated based on the measured count rate using the conversion factors from counts/s pixel to kR determined by *Gustin et al.* [2012]. We note that they refer to the H_2 B $^1\Sigma_u^+ \rightarrow X\,^1\Sigma_g^+$ (Lyman bands) and $C\ ^1\Pi_u \rightarrow X\,^1\Sigma_g^+$ (Werner bands) emissions within the STIS spectral passband. Emission rate values without absorption for the full B→X and →X emission spectrum, including the wavelength range below Lyman α, may be estimated by multiplying the values quoted below by a factor depending on the observed color ratio. This factor is close to 2 for unabsorbed regions and increases with the color ratio. An example of two spectra obtained on 8 January in two different regions of the main auroral emission is given in Figure 1, following normalization of the intensity in the unattenuated long-wavelength region. The difference in the amount of absorption by methane is clearly observed below about 150 nm. Further discussion of these spectra is given in section 4.1.

4. Spectral Images

We now describe the auroral images reconstructed on the basis of the time-tagged data collected during the slit scans of the polar regions using the method described in section 3 to determine the coordinates of each image pixel.

4.1. The 8 January Image

The reconstructed spectral image collected on 8 January in the Northern Hemisphere is shown in Figure 2a obtained by addition of photons collected in the (unabsorbed) 155–162 nm region. Its polar orthographic projection is shown in Figure 2b. The dotted or dashed lines indicate the meridians and the parallels,
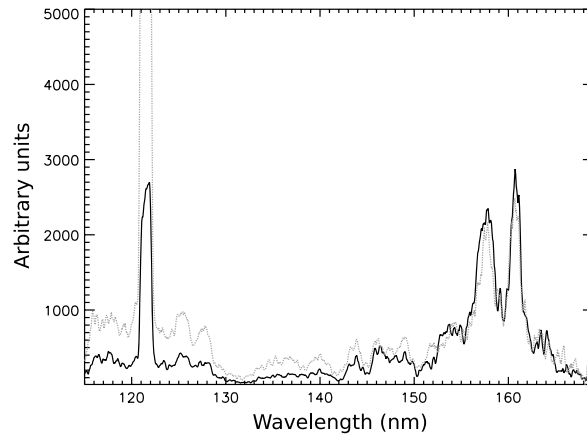
Figure 1. Auroral spectra obtained on 8 January 2014 in two different zones of the main auroral emission. The dotted line represents the average spectrum in zone A (noon sector). The black solid line corresponds to zone B (morning sector). The two spectra have been normalized between 155 and 162 nm. The enhanced absorption in zone B is a clear signature of the larger amount of hydrocarbons, mainly methane, overlying the aurora in comparison with zone A.

whilethe solid white lines show the statistical location of the Io auroral footprint [*Bonfond et al.*, 2009] and of the main emission [*Bonfond et al.*, 2012]. Both figures exhibit the usual features of the northern FUV aurora collected previously by cameras on board the HST. The Io footprint, marked with yellow arrow (1) and its trailing tail are aligned along the statistical oval of the footprint as it defined by a large number of FUV auroral images [*Bonfond et al.*, 2009]. The tail is seen as far as the night limb where it vanishes. The brightness of the main emission is nearly constant along the planetary limb but it strongly varies on the dayside. A brighter region (arrow 2), where the H_2 emission reaches 1.4 MR, extends over approximately 15° of longitude in the morning sector with an intensity decreasing toward the 180° S_{III} meridian. It shows a series of striations quasi-aligned with the
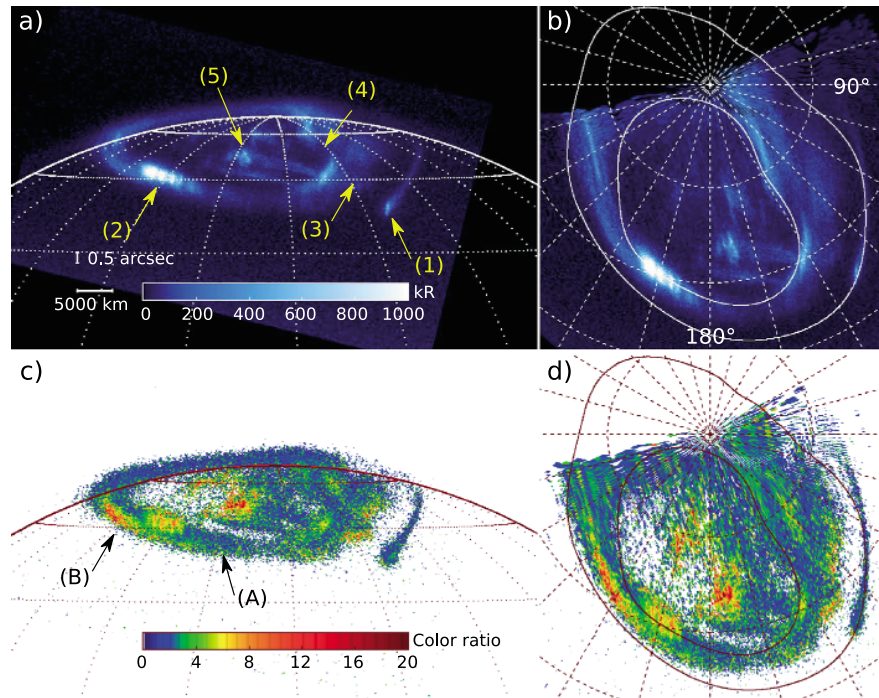
Figure 2. (a) Reconstructed north auroral image based the STIS spatial scan performed on 8 January 2014. Parallels and meridians are shown every 15° by the white dotted lines. The projected size of the 0.5 arc sec STIS slit and a 5000 km distance is indicated in white on the disk. Auroral regions described in the text are shown by yellow arrows. (b) Polar orthographic projection of the same data. The 180° S_{III} meridian is toward the bottom, the morning sector is to the left and evening to the right. The inner white line represents the statistical location of the main emission, and the outer line shows the position of the Io footprint. (c) Observed FUV color ratio corresponding to Figure 2a. The black arrows indicate the two areas used to construct spectra in Figure 1. (d) Polar orthographic projection of the observed color ratio. The dark solid lines show the statistical location of the main emission and of the Io footprint.

local S_{III} meridian near $\lambda_{III} = 195°$. As typically observed in auroral images taken from Earth orbit in the vicinity of this central meridian longitude (168°), the main emission intensity drops in the noon sector and broadens at smaller longitudes, with no bright arc structure observed in the late afternoon at S_{III} longitudes less than about 160°. It leads the way to an emission region (arrow 3) extending between the statistical location of the main emission shown by the white line and the Io tail region. A region with weak diffuse emission is also seen in the high-latitude morning sector with a narrow extension down to the 165° meridian. A second dark area is located near 150° (arrow 4), poleward of several broad regions of auroral emissions that are present at high latitudes, especially in the noon and afternoon sectors. Several polar bright regions are seen inside the main emission. These features and their characteristics have been abundantly described in the literature, and their structure was analyzed by *Grodent et al.* [2003] who proposed a classification based on their statistical behavior. A dramatic example of a strong auroral enhancement was described by *Waite et al.* [2001], and the temporal variations of some of these features in the south were analyzed by *Bonfond et al.* [2011].

Figure 2c presents the observed spatial distribution of the color ratio calculated according to formula (1), and Figure 2d shows the corresponding polar projection. It is important to note that contrary to the filtered true images previously obtained with HST, all wavelengths in the STIS spectra are simultaneously observed, so that, even in the presence of time varying brightness and/or structure, the color ratio is a true indicator of the instantaneous depth of the aurora relative to the methane homopause. Several remarkable features are readily seen:

1. The color ratio varies over a wide range from 1.5 near the nightside limb and along the Io trailing tail up to values as large as 28 in the bright polar spot near the 180° S_{III} meridian in the polar region (arrow 5). Values of the color ratio up to 10 are also measured in the striations in the morning main emission near 195° and near the equatorward boundary of the main emission between 200° and 230° in the morning sector. Spectra have been extracted for two regions along the main emission. Zone A extends between 165° and 190° S_{III} longitudes in the noon sector while zone B is in the morning sector between 210° and 245°. Both zones are approximately 5° of latitude wide. Spectra corresponding to these two regions have been built up by summing the signal of all pixels within these zones. They have been normalized to the total number of counts between 152 and 165 nm following correction for the response of the STIS instrument in the G140L spectral mode. They are shown in Figure 1 in dotted and solid and lines respectively. The observed color ratios are 4 in zone A and 1.5 in zone B, indicating a harder precipitation on the morning side, in agreement with Figures 2c and 2d. The quantitative implications of these differences will be discussed in the next section.
2. The highest values of the color ratio may or may not coincide with the brightest regions. The structure of the bright streaked region in the morning sector and the bright polar spot near 195° is positively correlated with values of color ratio which varies between 10 and 5 in and between the streaks. By contrast, the Io footprint and the two diffuse regions located in the afternoon sector poleward of the Io tail exhibit a low color ratio.
3. The polar emissions show a strongly inhomogeneous color ratio ranging from less than 2 to 28, indicating a wide range of mean electron energy in the electrons precipitated inside the main emission. Some of the image regions with the highest-color ratios are located in these diffuse high-latitude regions, a clear signature of the presence of a strong but variable acceleration process along their magnetic field lines.
4. The two bright regions (arrow 3) in the morning sector between the main emission and the Io tail, possibly associated with plasma injection from the middle magnetosphere, show a harder precipitation near their dayside boundary.

4.2. The 14 January Image

The CML during this spatial scan was 242° S_{III} at the beginning of the exposure. As mentioned before, this HST visit partly missed the target, so that part of the afternoon and the evening sectors of the northern emission were not observed. As in Figure 2, Figures 3a and 3b show the intensity distribution and Figures 3c and 3d the distribution of the color ratio. We note that the geometry of this observation is less favorable than on 8 January, so that the projected slit width significantly degrades the spatial resolution. The auroral emissions show less intensity contrast between the different regions, possibly an effect of the spatial smoothing. Nevertheless, the main emission is clearly apparent from the morning limb to the edge of the image in the afternoon sector. The Io magnetic footprint is seen near 205° S_{III} (arrow 1) but its tail rapidly merges with the main auroral emission and becomes indistinguishable.
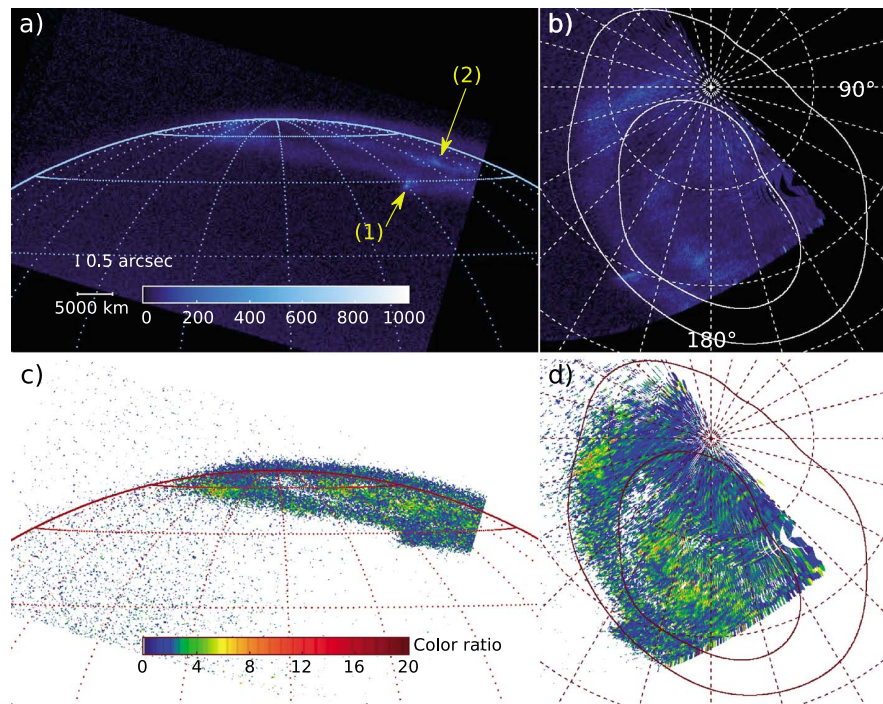
Figure 3. Observations based on the STIS spatial scan performed in the north on 14 January 2014. (a) Observed image and (b) its polar projection. (c) The observed color ratio and (d) its polar projection. See Figure 2 for further details.

The range of variation of the color ratio is also more limited here than on the 8 January image, with values of less than 2 up to 9 in the brighter morning region near 280° S_{III}. The polar emission (arrow 2) shows color ratio values in the range 3 to 7 with a morphology resembling that of the intensity distribution in Figures 3a and 3b. As previously, the Io footprint is associated with a low value of the color ratio.

4.3. The 15 March Image

This Northern Hemisphere exposure was made for a CML longitude of 220° at scan start, a value midway between the previous two images. Figures 4a and 4b represent the brightness, and Figures 4c and 4d represent the color ratio distribution observed during this visit. The highest intensities are located in the 200°–210° S_{III} range (arrow 1) near noon and the afternoon 150°–170° (arrow 2) sectors. A bright region of diffuse aurora is seen near the morning limb, equatorward of the main oval (arrow 3). The signature of the Io footprint is observed on the duskside near the nightside limb (arrow 4). The second brightening located slightly south of the footprint (arrow 5) is not associated with the position of any magnetic tube connected to a Galilean satellite and is probably caused by plasma injection mapping equatorward of the main emission, that is at a radial distance between Io's orbit and 20–30 Jovian radii in the equatorial plane. Diffuse emission almost entirely fills the polar region, although it remains weaker than the main emission.

The color ratio distribution is represented in Figures 4c and 4d. The values vary from about 1.5 at the nightside limb up to a maximum pixel value located in the polar region of 21, or 13 if the image is first smoothed over a 3 × 3 pixel square. Comparison of the color ratio map with the emission brightness indicates several interesting features.

1. High values of the color ratio on the main oval correspond to regions of relatively high auroral emission rate. This is however not verified near the morning limb where only the equatorward edge of the arc corresponds to increased color ratios.
2. Globally, the morning sector of the main emission does not show an increased color ratio, unlike the 8 January image.
3. As on 8 January image, the highest-color ratio values are observed in the polar emission and correlate well with regions of modest enhancement of the auroral brightness.
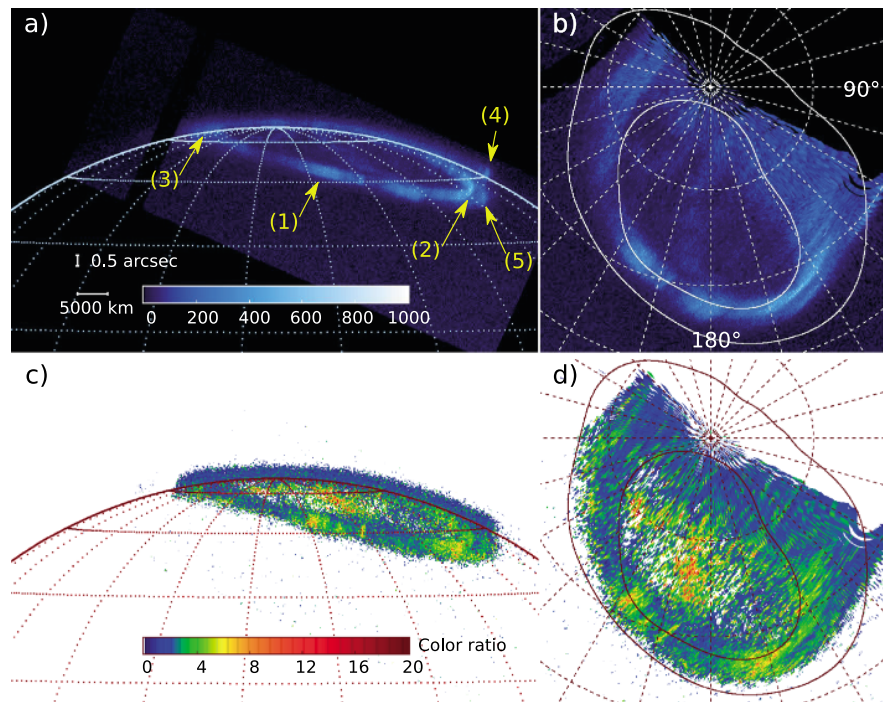
Figure 4. Observations based on the STIS spatial scan performed in the north on 15 March 2014. (a) The observed image and (b) its polar projection. (c) The observed color ratio and (d) its polar projection. See Figure 2 for further details.

4. The footprint brightness signatures do not exhibit enhanced values of the color ratio.

4.4. The 12 January Image

This is the only exposure obtained while observing the south polar region. It was collected with a CML at scan start of 37° in order to optimize the less favorable view of the southern high-latitude regions. Figures 5a and 5b show that the main emission is detected from the dawn to the dusk limb, although the auroral brightness is inhomogeneous along the arc, with significant brightening in the dusk sector (arrow 1). A latitudinally extended region of diffuse aurora is observed in the morning sector (arrow 2), and a zone of relatively bright emission (arrow 3) crosses the polar region from the night limb near 340° S_{III} to reach the main emission between 45° and 60°.

The color ratio measured near the dawn limb at 75° S_{III} longitude reaches values as high as 40 in the brightest pixels and 29 in the smoothed image. These are the highest values of all four observations. As in the other exposures, the color ratio at the limb is less than 2, while the transpolar feature has a color ratio on the order of 5, with peak values up to 11.

Finally, the Ganymede footprint is observed on the dusk limb (arrow 4) with a slant intensity of about 400 kR and a color ratio of 1.8, similar to the Io footprint value.

5. Numerical Simulations of the Color Ratio

A determination of the depth of the aurora relative to the methane homopause can be made from the amount of absorption in the FUV spectra. The method is related to the large drop in the CH_4 absorption cross sections at wavelengths higher than 140 nm, leaving the longer wavelength H_2 Lyman band unattenuated, while the emissions at shorter wavelengths are significantly absorbed by methane and, to a lesser degree, other hydrocarbons. Therefore, the altitude of the auroral emitting layer relative to the methane homopause, and thus the electron energy, may be derived from the observed spectrum. The method to analyze the color ratio in terms of auroral depth in the atmosphere was described by *Gérard et al.* [2013] and is briefly summarized below. The unabsorbed synthetic spectrum calculated under optically thin conditions is used to simulate the auroral source. It was shown to be fully consistent with the laboratory spectrum obtained by bombarding a cell filled with low pressure H_2 with 100 eV electrons [*Dziczek et al.*, 2000]. A Monte Carlo electron transport code
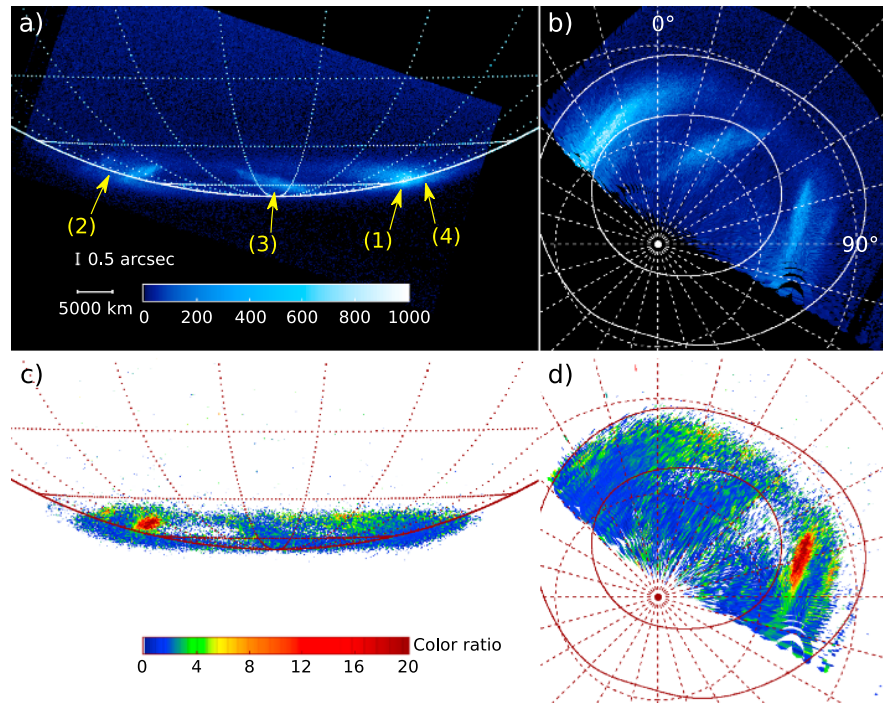
Figure 5. Observations based on the STIS spatial scan performed in the south on 12 January 2014. (a) The observed image and (b) its polar projection. (c) The observed color ratio and (d) its polar projection. See Figure 2 for further details.

[*Gérard et al.*, 2009, 2013; *Bonfond et al.*, 2009] is used to calculate the H_2 Lyman and Werner volume emission rate for a series of initial electron beams with prescribed energy distribution at the top of the model. Electron transport is described by the Boltzmann kinetic equation, which is numerically implemented using the Direct Simulation Monte Carlo method used to solve atmospheric kinetic systems in the stochastic approximation. The electrons are assumed to be isotropically distributed over the downward hemisphere at the upper boundary of the model. In summary, the initial energetic electron beam and the secondary electrons created following ionizing collisions interact with the ambient neutrals and lose their excess kinetic energy in elastic, inelastic, and ionizing collisions with the H_2 molecules and H and He atoms. The cross sections and scattering angle laws to calculate the energy loss associated with elastic and inelastic collisions of electrons were described by *Gérard et al.* [2013]. The model was updated for this study to extend the cross section to the range of relativistic electron energies. The lower boundary corresponds to the 1 bar level, and the upper boundary is located at 1400 km or 1×10^{-10} bar in Moses et al.'s model, where collisions with the atmospheric gas become very rare. The evolution of the system of modeled particles due to collisional processes and particle transport is calculated from the initial to the steady state. In a first step, we use the neutral model atmosphere derived by *Moses et al.* [2005], including their hydrocarbon density profile. The eddy diffusion coefficient including its pressure dependence is described in *Moses et al.*'s [2005] model B and shown in their Figure 7. It provides a reasonable fit to the spectral observations of C_2H_2 and C_2H_6 bands made with the Infrared Space Observatory (ISO) satellite.

The auroral model calculates the volume emission rate profile for the H_2 Lyman and Werner bands (B and C singlet states) by folding the appropriate excitation cross sections with the calculated total electron energy spectrum in each altitude bin for each incident electron flux distribution. Examples of the distribution of the volume emission rate of the total B-X and C-X H_2 emissions calculated with the Monte Carlo model are shown in Figure 6 on a vertical scale in pressure units. Subsequently, the emergent intensity per unit interval I_λ at wavelength λ along any given line of sight is numerically calculated as

$$I_\lambda = \int P_\lambda(z) \; e^{-\tau_\lambda} ds, \qquad (2)$$

where $P_\lambda(z)$ is the total volume emission rate of the H_2 B → X and C → X transitions at wavelength λ and altitude z with the spectral distribution of the laboratory reference spectrum. The slant integral (represented
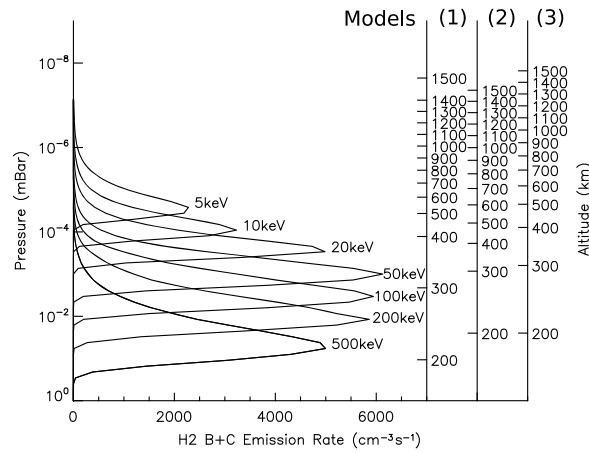
Figure 6. Vertical distribution of the total (B-X and C-X) H_2 volume emission rate (in $cm^{-3} s^{-1}$) calculated using a Monte Carlo code for monoenergetic beams of auroral electrons carrying $1\,mW\,m^{-2}$ with energy values ranging from 5 to 500 keV. The curves are calculated in terms of pressure levels, but altitude scales are shown on the right. They correspond to atmospheric models 1, 2, and 3, respectively.

by coordinate s) extends along the line of sight from the bottom of the auroral emission layer up to the top of the model. The optical depth at wavelength λ overlying altitude z is denoted $\tau_\lambda(z)$ and is given by
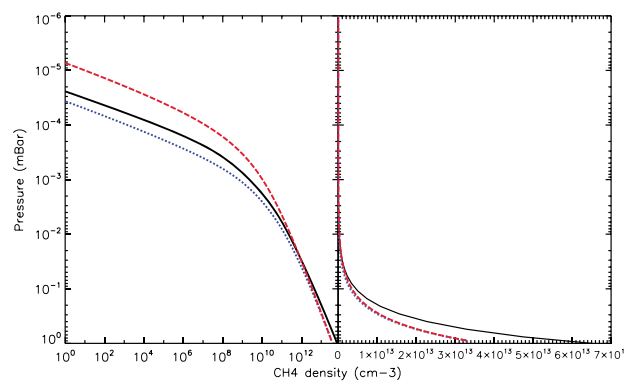
$$\tau_\lambda(z) = \sigma_\lambda(CH_4) \int_z^\infty n_{CH_4} ds, \qquad (3)$$

where $\sigma_\lambda(CH_4)$ is the methane absorption cross section at wavelength λ, n_{CH_4} is the local number density of methane, and ds is again the path length along the line of sight. The energy distribution of the precipitating electrons is arbitrarily prescribed, but, given the uncertainties in this distribution and other sources of errors, most simulations were performed with monoenergetic electron beams. The sensitivity to this assumption will be discussed in section 6.

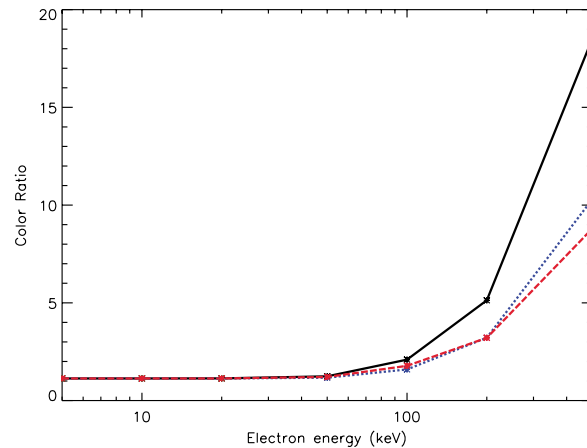Each pixel of the reconstructed image has its own viewing geometry with a corresponding emergent spectrum, which makes the simulations complex. Therefore, for simplicity of analysis, the FUV color ratio CR given in formula (1) is calculated for each simulated pixel of all four images for different initial electron energies E_0. A curve relating the color ratio value to the initial energy E_0 is obtained for a given model atmosphere by interpolating between a discrete number of numerical simulations.

The observations of the Jovian aurorae performed by the HST were made at a range of slant angles, and this angle varied from one location on the planet to another. This angle affects both the accumulation of light emission and the accumulation of absorbent along the line of sight. Assuming a spherically homogeneous emitting shell, we computed the color ratio corresponding to the different electron energies for angles ranging from 0 to 90°. Knowing the location of the planetary center on the pseudoimages, the slit orientation and the plate scale, it is possible to compute the angle between the observer and the normal to the surface for each point. Then from this angle and the measured color ratio, we inferred the electron energy. Since the relationship between the color ratio and the initial energy depends on the vertical distribution of hydrocarbons (mostly methane, but we also included C_2H_2 in our simulations), we made some simulations with different model atmospheres to assess the resulting uncertainties of the initial electron energy. As mentioned before, we start with *Moses et al.* [2005] model B, named here model 1, which is based on the hydrocarbon distribution derived from the ISO satellite measurements at low latitudes and is quite similar to *Gladstone et al.*'s [1996] profile. The eddy diffusion coefficient K_H at the methane homopause is close to $3 \times 10^6\,cm^2\,s^{-1}$. We also use atmospheric density profiles from the one-dimensional auroral model of *Grodent et al.* [2001] which self-consistently solved the atmospheric heat and the diffusion equations. We adopt their model where the eddy diffusion coefficient at the homopause K_h is equal to $1.4 \times 10^6\,cm^2\,s^{-1}$ and use it as our standard case, under the name model 2. As a sensitivity test we compare the energy-color ratio relationship with that

Figure 7. Vertical distribution of the methane number density versus pressure for three different atmospheric models (see text): 1 (black solid line), 2 (dotted blue line), and 3 (dashed red line). (left) Logarithmic methane density scale. (right) Linear density scale.

Figure 8. Variation of the FUV color ratio (I(155-162)/I(123-130)) calculated as a function of the initial electron energy for a view angle of 60°. The colors correspond to model atmospheres 1 (black solid line), 2 (dotted blue line), and 3 (dashed red line) (see text).

obtained using Grodent et al.'s atmosphere for $K_h = 1.4 \times 10^7$ cm^2 s^{-1} (model 3) to cover a range from a typically low latitude value (see discussion by *Moses et al.* [2005]) up to a value 10 times as high. The latter value of the strength of eddy mixing is believed to represent an upper limit to the conditions prevailing in the auroral zone. An increase of the eddy mixing efficiency in the auroral regions was suggested by *Parkinson et al.* [2006], who derived a value of 8×10^6 cm^2 s^{-1} and possibly larger on the basis of the HeI 58.4 nm airglow distribution observed with the Ultraviolet Imaging Spectrograph during the flyby of Jupiter by Cassini. The methane number density profile for the three models is shown in Figure 7 as a function of the pressure level in both logarithmic and linear scales.

We note that the differences between the models by Moses et al. and Grodent et al. stem not only from the different vertical profiles of the eddy diffusion coefficient but also from the thermal structure and the pressure-altitude relationship related to the auroral heat source. In the simpler case of a fixed thermal profile and neutral background atmosphere, the sensitivity of the color ratio-electron energy dependence to the value of K_H was illustrated in *Gérard et al.*'s [2003] Figure 2. The higher the value of K_H, the more abundant the hydrocarbon density above the homopause and the lower the value of the incident electron energy for a given color ratio. The dependence of the calculated color ratio versus the (monoenergetic) initial electron energy is illustrated in Figure 8 for the case of a view angle of 60°, for the three different model atmospheres described before. As expected, the color ratio strongly varies for electron beams with an initial energy higher than about 50 keV, and, for a given value of the initial electron energy, it depends on the adopted model atmosphere. It remains close to the unabsorbed value of 1.1 for energies less than 50 keV, as most of these electrons are stopped above the methane homopause in all three atmospheric models. We also note that the curves corresponding to models 2 and 3 show only slight differences. Comparing with the methane distribution shown in Figures 7a and 7b, the reason for this similarity is clear: the two methane density profiles only differ significantly at pressure levels less than 10^{-2} mbar, a region where the CH$_4$ density, and thus the absorption, is vanishingly small.

6. Maps of the Electron Characteristic Energy

We first concentrate on the electron energy map derived from the slit scan of 8 January 2014 and examine the spatial distribution of the electron energy for the three atmospheric models described in section 5. Figure 9 shows the maps of the characteristic electron energy (assumed to be monoenergetic) corresponding to the color ratio distribution displayed in Figure 2 where we show the view from Earth orbit on the left and the polar projection on the right. As mentioned before, the highest-color ratio is observed in the polar emission and corresponds to a primary auroral electron energy E_0 ranging from 400 keV with model 1, to 670 keV in model 2 and to over 825 keV in model 3. We note that, globally, the electron energies are slightly higher for model 3 than model 2, although the value of the eddy diffusion coefficient is 10 times higher. This is a consequence of the interplay between the increasing cooling rate caused by the larger methane density which, in turn, modifies the thermal structure of the upper atmosphere in the Grodent et al. model.

The highest E_0 value in the morning sector of the main oval is close to, but slightly less than in the high-latitude spot. Typical values in the main oval near the central meridian (noon sector) vary from 100 to 150 keV with models 1 and 2, to 100–300 keV with model 3. The lowest auroral energies correspond to the nightside limb observations with energies below 60 keV in all three cases. We note that the electron energy associated with the Io footprint is about 100 keV and appears slightly higher than in the trailing tail. Such large values were
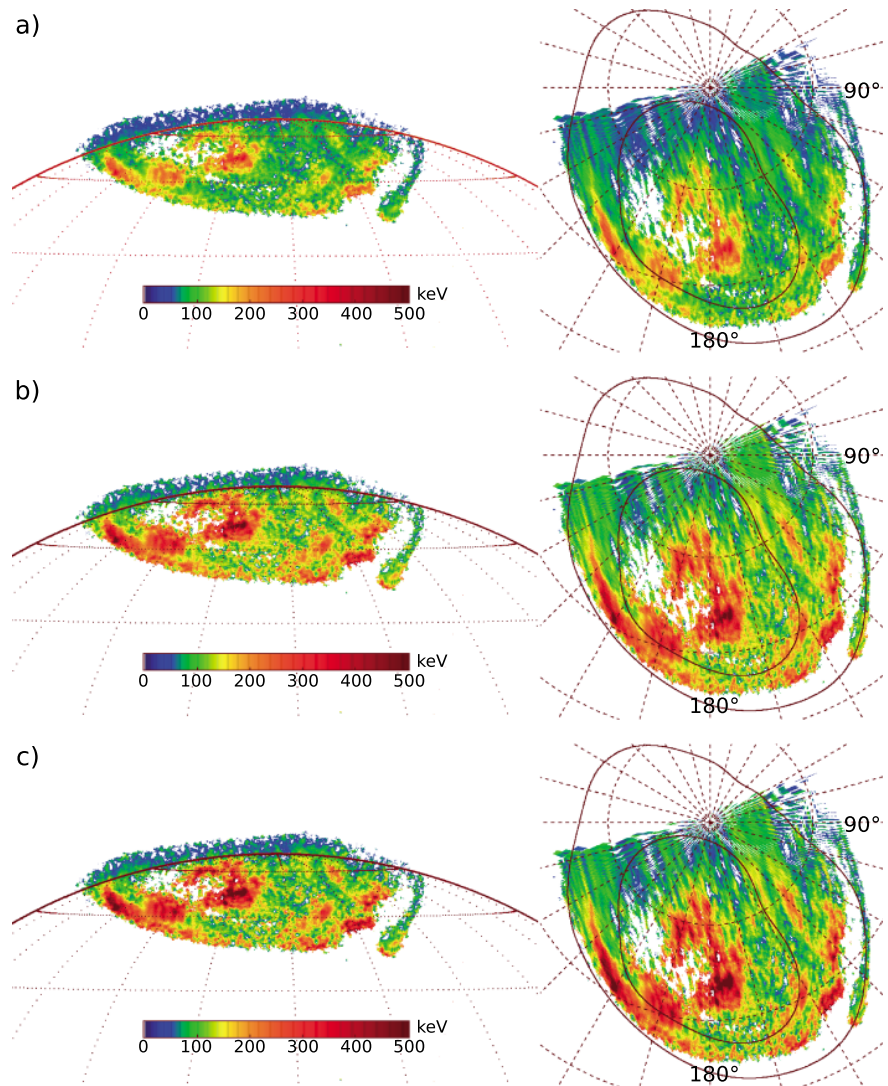
Figure 9. Distribution of the electron characteristic energy for the aurora observed on 8 January 2014. The three sets correspond to different atmospheric models: (a), model 1, (b) model 2, and (c) model 3. The Figures on the left side correspond to the view from Earth orbit, while those on the right side are polar orthographic projections of the same data. The 180° S_{III} meridian is toward the bottom, the morning sector is to the left and evening to the right. The inner dark red line represents the statistical location of the main emission and the outer line shows the statistical position of the Io footprint.

previously derived from STIS spectral observations [*Gérard et al.*, 2002] but are incompatible with the altitude of ~900 km observed on images of the footprint at the limb from which *Bonfond et al.* [2009] derived a mean energy of 1–2 keV. They are also incompatible with currently accepted models of the acceleration in the Io flux tube [*Hess et al.*, 2013]. It is not clear why the two methods yield such widely different energy estimates.

To facilitate comparisons with earlier electron energy determinations from STIS spectral measurements available in the literature, we focus on the energy maps calculated with model 2 (*Grodent et al.*'s [2001] standard auroral model) whose parameters were adjusted to match temperature and composition constraints. Figure 10 summarizes the energy maps derived from the 2014 HST set of spectral scans. We first concentrate on the global energy morphology observed in the polar projections of the northern aurora. Unexpectedly, it is clearly seen that although the absolute intensity and energy vary from one case to another, the location of the regions of high-energy precipitation is well defined when displayed in S_{III} longitude. It is characterized by high E_0 values along the main emission zone, and the presence of an
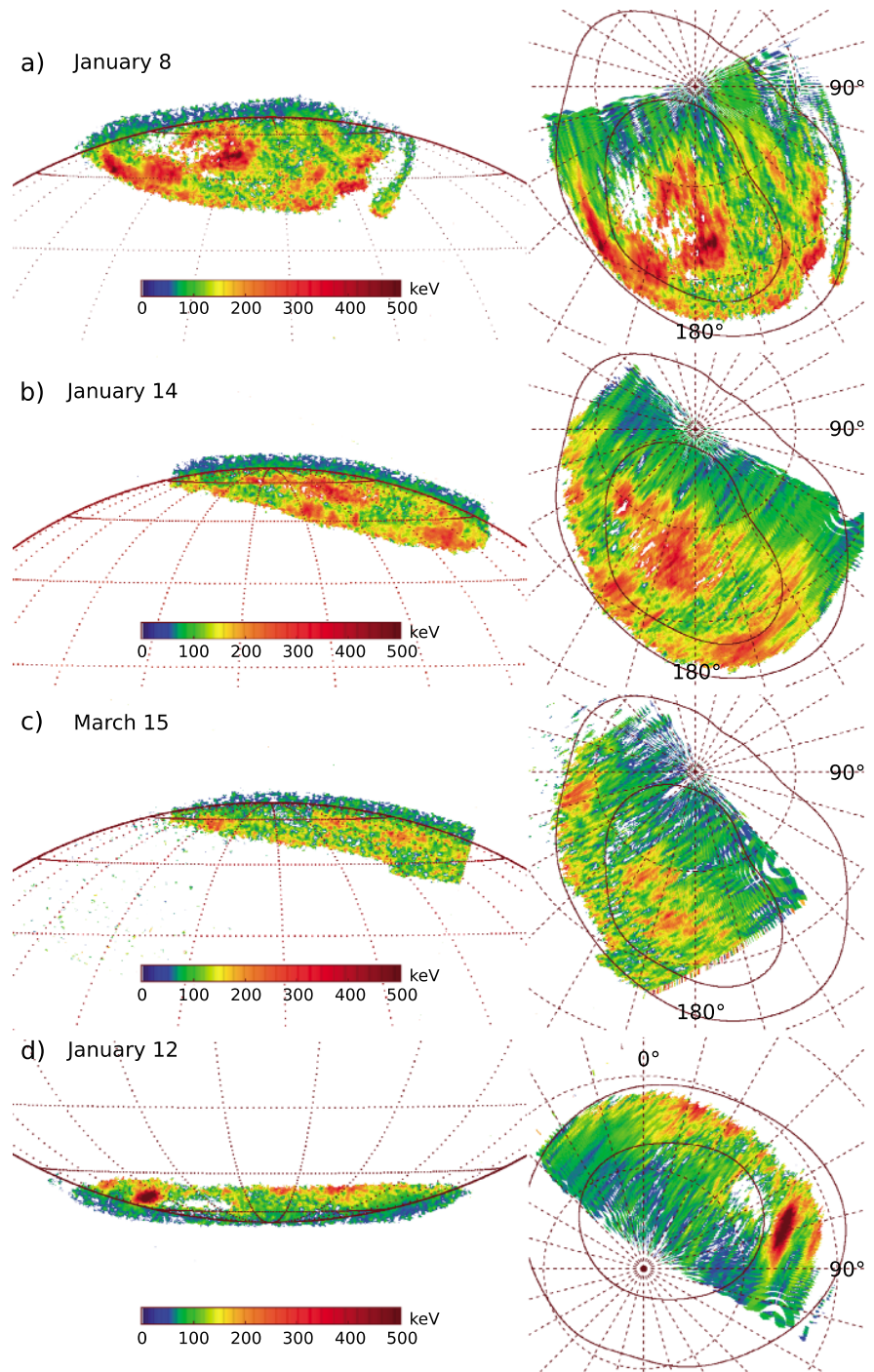
Figure 10. (left column) Distribution of the electron energy for the aurora for the four HST visits using model atmosphere 2 (see text). (right column) Polar projection of the same data. The 180° S_{III} meridian is toward the bottom, the morning sector is to the left and evening to the right. The inner dark red line represents the statistical location of the main emission, and the outer line shows the statistical position of the Io footprint.

extended region of diffuse hard precipitation in a broad sector between roughly 160° and 250° S_{III}. The comparison of the observed structures in local time (left) and S_{III} distribution (right) in Figure 9 suggests that the bulk of the polar precipitation is located in the active region where bright polar flares have been observed [*Waite et al.*, 2001; *Grodent et al.*, 2003].

Another interesting feature, most clearly seen in Figures 9a and 9b, is the series of "beads" observed in the morning sector between 180° and 200° S_{III} longitude. The brightness modulation seen in Figure 2 is also observed in the corresponding values of E_0, with a positive correlation between the brightness and the mean energy that varies between 100 and 250 keV for atmospheric model 2. We also note the presence of two regions associated with enhanced brightness and electron energy in the afternoon sector, near 140° and 160°, equatorward of the main emission and poleward of the Io auroral tail. These structures are reminiscent of the signatures of transient plasma injections first described by *Mauk et al.* [2002b] and analyzed statistically by M. Dumont et al. (Jupiter's equatorward auroral features: Possible signatures of magnetospheric injections, submitted to *Journal of Geophysical Research: Space Physics*, 2014). The mean electron energy is significantly higher in these two bright spots than in the surrounding diffuse emission, with values of E_0 in the range 200–300 keV. These values are within the range (from ~20 to 700 keV) of the electron peak energy measured by *Mauk et al.* [2002b] in the equatorial plane for the dispersion event they observed on day 363 of 2000.

Although the CML was selected to offer an optimal view of the southern aurora, the energy information in Figure 10d is less detailed than in the north. It indicates that the characteristic electron energy may locally exceed 500 keV near the morning limb at longitudes between 65° and 90°. Elsewhere along the main emission, the values of E_0 are on the order of 100 keV or less.

We now examine the sensitivity of the color ratio-energy relationship on the shape of the energy distribution spectrum. Depending on the plasma source region and the acceleration processes involved, the energy distribution may be essentially mononergetic (accelerated by a confined voltage drop along the field lines), Maxwellian (accelerated followed by scattering due to wave-particle interaction above the ionosphere), or some other shape. As a sensitivity test, we compared the color ratio associated with a monoenergetic and a Maxwellian distribution having identical mean electron energy. For example, for a mean energy of 50 keV, the color ratio for a view angle of 60° is 1.2 in the monoenergetic case and 1.5 for a Maxwellian energy distribution. Inversely, if the distribution is actually Maxwellian but assumed to be monoenergtic, the energy associated with a color ratio of 1.5 would be 50 keV instead of 79 keV in the Maxwellian case. As mentioned before, in the absence of in situ measurements below the acceleration region, we simply assumed in this work that the auroral precipitation is monoenergetic in all regions.

In comparison to earlier measurements made over limited spatial regions, the values observed in Figure 10 are in general agreement with those observed with GHRS and STIS on board HST. However, the present two-dimensional images identify localized regions, both along the main emission and in the polar region whose color ratio and electron energy exceed the values previously observed.

7. Summary and Conclusions

Spectral images of Jupiter's ultraviolet aurora obtained with the STIS imaging spectrograph on board HST have provided the first two-dimensional maps of absorption of the H_2 FUV emission by methane and ethylene, a proxy for the penetration depth of auroral electrons. The exposures were made for different central meridian longitudes in the north and an optimal view in the south. They show that absorption by methane varies along the main emission and between the various components of the aurora. These results indicate that the penetration depth of auroral electrons changes with time and location. The most energetic precipitation appears to be associated with some of the polar flares observed at high latitudes, inside the main emission region. Therefore, the concept of a "global" auroral color ratio with no spatial resolution has little significance as it mixes different regions characterized by different electron energies, possibly powered by unrelated acceleration mechanisms.

Based on the methane vertical distribution adapted to polar latitudes and on a Monte Carlo code simulating the auroral emission from electron precipitation, we derive mean electron energies ranging from less than 50 keV up to over 500 keV, which sets the pressure level of the auroral peak between less than 9.1×10^{-4} and 5.8×10^{-2} mbar, corresponding to 320 and 215 km, respectively, in the atmospheric model by *Moses et al.* [2005]. We stress that, by contrast to the color ratio maps of Figures 2–5 which are directly derived from the observations, maps of the characteristic electron energy (Figure 9 and 10) require the combination of an electron transport model with a model atmosphere. The relationship between the color ratio and the electron energy depends on the vertical distribution of the methane mixing ratio, a quantity that has not been directly measured in the

high-latitude upper atmosphere of Jupiter. If, for any reason, this mixing ratio dropped less rapidly than assumed in the models used in this study, the derived electron energy would be lower that values illustrated.

We also note that the energy-flux relationship by *Knight* [1973] is no longer valid for relativistic electron energies ($E_0 > \sim 100$ keV). Formulae based on the Knight model adapted to the relativistic case were given by *Cowley* [2006], following observations of very high color ratios during Jovian morning storms. For relativistic accelerating potentials along the field lines, the current density increases as the square of the minimum potential, rather than linearly as in the nonrelativistic regime, while the kinetic energy flux then increases as the cube of the potential, rather than as the square.

Comparison between the four reconstructed images in Figure 10 indicates that the harder precipitation observed on 8 January 2014 in the morning sector of the main emission (Figures 2, 9, and 10a) at S_{III} longitudes larger than 180° does not appear to be a fixed S_{III} longitudinal feature. The other spectral images collected at different central meridian longitudes do not show any energy enhancement specifically associated with this sector. The 14 January reconstructed image does not show any enhanced sector of the main emission with the exception of the spot in the 280° (morning) S_{III} sector. The 15 March data show the presence of softer precipitation in the morning sector but large value of E_0 in the vicinity of the 210° S_{III} region. The highest energies are seen in the morning region near 90° in the Southern Hemisphere.

Nichols and Cowley [2004] were able to explain the characteristics of the main emission aurora using the *Cowley and Bunce* [2001] physical concept and including a Pedersen conductivity modified by the energy flux of the precipitating electrons. They determined the energy flux of the precipitating electrons by using the linear approximation of the *Knight* [1973] formula to relate the current density to the field-aligned potential. *Ray et al.* [2010] developed a model merging the physics described by *Nichols and Cowley* [2004] by both self-consistently including field-aligned potentials in the electric field mapping and varying the Pedersen conductivity with electron precipitation. This time-independent model of Jupiter's rotation-driven aurora is based on angular momentum conservation, including the effects of a field-aligned potential and changes in the ionospheric conductivity modified by the auroral precipitation. They applied a current-voltage relation, taking into account the low-plasma densities at high latitudes. Their model could quantitatively reproduce most features of Jupiter's main auroral oval, including the energy flux into the ionosphere, the width of the aurora ionosphere, and the net radial current across the field. They showed that the accelerating potential energy for a given rate of plasma radial transport and thus the auroral electron energy strongly depend on the location of the acceleration region. For an iogenic neutral material production rate of 500 kg s^{-1} and a total radial current at 100 R$_J$ equal to 86 MA, the modeled auroral oval has a peak energy flux of 23 mW m^{-2} and a peak precipitation electron energy of $\sim$115 keV mapping to $\sim$40 R$_J$. In a subsequent study, *Ray et al.* [2012] analyzed the sensitivity of their model to various assumptions but essentially confirmed the results by *Ray et al.* [2010]. The range of energies in the main emission region derived from this work overlaps the model values but locally exceeds the modeled values.

In the polar region, the only detailed conceptual model was developed by *Bunce et al.* [2004] for the cusp precipitation. They considered "slow" and "fast" flow models corresponding to low and high values of the interplanetary magnetic field strength, respectively, of the twin-vortical flows which occur as a result of pulsed dayside reconnection and the associated bipolar field-aligned currents. The calculated voltage associated with the "slow flow" was 34 keV, and 90 keV with the "fast flow" model for downward acceleration along closed field lines. The calculated values were substantially less along open field lines. The highest characteristic energies we deduce from the polar observations are substantially higher, but the corresponding auroral brightness, and thus the associated downward current, is also larger than the modeled brightness.

In this analysis, we have assumed that only energetic auroral electrons carry the energy flux which ultimately produces FUV photons. There is also a possibility that precipitating energetic ions associated with downward current regions in the polar region also contribute to the H$_2$ emission through secondary electrons produced along their atmospheric path. *Branduardi-Raymont et al.* [2008] measured X-ray emission along and inside the main emission. The high-latitude emission was interpreted as the signature of precipitating oxygen and sulfur or carbon ions of several MeV energy. The efficiency of energetic oxygen ions in producing FUV photons was modeled by *Ozak et al.* [2013] who calculated an average H$_2$ emission rate of 80 kR for the polar X-ray emission. Although this brightness is less than the several hundreds of kR H$_2$ emission generally associated with the bright polar spots, it is possible that heavy energetic ion precipitation contributes to the excitation of the high-latitude aurora.

UV spectral scans with increased spatial resolution will be obtained with the UVS instrument on board the Juno mission to Jupiter [*Gladstone et al.*, 2014]. In addition to the improved instrumental performance, in situ measurements of the auroral electron flux will be performed simultaneously with spectral imaging covering the region of the footprint of the magnetic field line crossing the spacecraft position. If these measurements are made below the electron acceleration region, as suggested by models which locate the acceleration region a few Jovian radii from the planet, a direct comparison will be made between the energy flux distribution, the auroral brightness, and the FUV color ratio. Such observations will also show whether the atmospheric model and the hydrocarbon distribution used in the present study are consistent with these concurrent observations.

References

Achilleos, N., S. Miller, J. Tennyson, A. D. Aylward, I. Mueller-Wodarg, and D. Rees (1998), JIM: A time-dependent, three-dimensional model of Jupiter's thermosphere and ionosphere, *J. Geophys. Res.*, *103*(E9), 20,089–20,112, doi:10.1029/98JE00947.

Ajello, J. M., et al. (1998), Galileo orbiter ultraviolet observations of Jupiter aurora, *J. Geophys. Res.*, *103*(E9), 20,125–20,148, doi:10.1029/98JE00832.

Badman, S. V., G. Branduardi-Raymont, M. Galand, S. L. G. Hess, N. Krupp, L. Lamy, H. Melin, and C. Tao (2014), Auroral processes at the giant planets: Energy deposition, emission mechanisms, morphology and spectra, *Space Sci. Rev.*, doi:10.1007/s11214-014-0042-x.

Bhardwaj, A., and G. R. Gladstone (2000), Auroral emissions of the giant planets, *Rev. Geophys.*, *38*(3), 295–353, doi:10.1029/1998RG000046.

Bonfond, B., D. Grodent, J.-C. Gérard, A. Radioti, V. Dols, P. A. Delamere, and J. T. Clarke (2009), The Io UV footprint: Location, inter-spot distances and tail vertical extent, *J. Geophys. Res.*, *114*, A07224, doi:10.1029/2009JA014312.

Bonfond, B., M. F. Vogt, J.-C. Gérard, D. Grodent, A. Radioti, and V. Coumans (2011), Quasi-periodic polar flares at Jupiter: A signature of pulsed dayside reconnections?, *Geophys. Res. Lett.*, *38*, L02104, doi:10.1029/2010GL045981.

Bonfond, B., D. Grodent, J.-C. Gérard, T. Stallard, J. T. Clarke, M. Yoneda, A. Radioti, and J. Gustin (2012), Auroral evidence of Io's control over the magnetosphere of Jupiter, *Geophys. Res. Lett.*, *39*, L01105, doi:10.1029/2011GL050253.

Bougher, S. W., J. H. Waite, T. Majeed, and G. R. Gladstone (2005), Jupiter thermospheric general circulation model (JTGCM): Global structure and dynamics driven by auroral and Joule heating, *J. Geophys. Res.*, *110*, E04008, doi:10.1029/2003JE002230.

Branduardi-Raymont, G., R. F. Elsner, M. Galand, D. Grodent, T. E. Cravens, P. Ford, G. R. Gladstone, and J. H. Waite Jr. (2008), Spectral morphology of the X-ray emission from Jupiter's aurorae, *J. Geophys. Res.*, *113*, A02202, doi:10.1029/2007JA012600.

Broadfoot, A. L., et al. (1981), Overview of the Voyager ultraviolet spectrometry results through Jupiter encounter, *J. Geophys. Res.*, *86*(A10), 8259–8284, doi:10.1029/JA086iA10p08259.

Bunce, E. J., S. W. H. Cowley, and T. K. Yeoman (2004), Jovian cusp processes: Implications for the polar aurora, *J. Geophys. Res.*, *109*, A09S13, doi:10.1029/2003JA010280.

Clarke, J. T., et al. (1996), Far-Ultraviolet imaging of Jupiter's aurora and the Io "footprint", *Science*, *274*, 404–409, doi:10.1126/science.274.5286.404.

Clarke, J. T., et al. (2002), Ultraviolet auroral emissions from the magnetic footprints of Io, Ganymede, and Europa on Jupiter, *Nature*, *415*, 997–1000.

Clarke, J. T., D. Grodent, S. W. H. Cowley, E. J. Bunce, P. Zarka, J. E. P. Connerney, and T. Satoh (2004), Jupiter's aurora, in *Jupiter: The Planet, Satellites and Magnetosphere*, edited by F. Bagenal, T. E. Dowling, and W. B. McKinnon, pp. 639–670, Cambridge Univ. Press, New York.

Clarke, J. T., et al. (2009), Response of Jupiter's and Saturn's auroral activity to the solar wind, *J. Geophys. Res.*, *114*, A05210, doi:10.1029/2008JA013694.

Cowley, S. W. H. (2006), Current-voltage and kinetic energy flux relations for relativistic field-aligned acceleration of auroral electrons, *Ann. Geophys.*, *24*, 325–338, doi:10.5194/angeo-24-325-2006.

Cowley, S. W. H., and E. J. Bunce (2001), Origin of the main auroral oval in Jupiter's coupled magnetosphere-ionosphere system, *Planet. Space Sci.*, *49*, 1067–1088.

Cowley, S. W. H., E. J. Bunce, and J. D. Nichols (2003), Origins of Jupiter's main oval auroral emissions, *J. Geophys. Res.*, *108*(A4), 8002, doi:10.1029/2002JA009329.

Dols, V., J.-C. Gérard, J. T. Clarke, J. Gustin, and D. Grodent (2000), Diagnostics of the Jovian aurora deduced from ultraviolet spectroscopy: Model and GHRS observations, *Icarus*, *147*, 251–266.

Dziczek, D., J. M. Ajello, G. K. James, and D. L. Hansen (2000), Cascade contribution to the H_2 Lyman band system from electron impact, *Phys. Rev. A*, *61*, 64,702-1–64,702-4.

Gérard, J.-C., V. Dols, F. Paresce, and R. Prangé (1993), Morphology and time variation of the Jovian far UV aurora: Hubble Space Telescope observations, *J. Geophys. Res.*, *98*, 18,793–18,801, doi:10.1029/93JE01334.

Gérard, J.-C., J. Gustin, D. Grodent, P. Delamere, and J. T. Clarke (2002), Excitation of the FUV Io tail on Jupiter: Characterization of the electron precipitation, *J. Geophys. Res.*, *107*(A11), 1394, doi:10.1029/2002JA009410.

Gérard, J.-C., J. Gustin, D. Grodent, J. T. Clarke, and A. Grard (2003), Spectral observations of transient features in the FUV Jovian polar aurora, *J. Geophys. Res.*, *108*, 1319, doi:10.1029/2003JA009901.

Gérard, J.-C., B. Bonfond, J. Gustin, D. Grodent, J. T. Clarke, D. Bisikalo, and V. Shematovich (2009), Altitude of Saturn's aurora and its implications for the characteristic energy of precipitated electrons, *Geophys. Res. Lett.*, *36*, L02202, doi:10.1029/2008GL036554.

Gérard, J.-C., J. Gustin, W. R. Pryor, D. Grodent, B. Bonfond, A. Radioti, G. R. Gladstone, J. T. Clarke, and J. D. Nichols (2013), Remote sensing of the energy of auroral electrons in Saturn's atmosphere: Hubble and Cassini spectral observations, *Icarus*, *223*, 211–221, doi:10.1016/j.icarus.2012.11.033.

Gladstone, G. R., M. Allen, and Y. L. Yung (1996), Hydrocarbon photochemistry in the upper atmosphere of Jupiter, *Icarus*, *119*, doi:10.1006/icar.1996.0001.

Gladstone, G. R., et al. (2014), The ultraviolet spectrograph on NASA's Juno mission, *Space Sci. Rev.*, doi:10.1007/s11214-014-0040-z.

Grodent, D. A. (2014), Brief review of ultraviolet auroral emissions on giant planets, *Space Sci. Rev.*, doi:10.1007/s11214-014-0052-8.

Grodent, D., J. H. Waite Jr., and J.-C. Gérard (2001), A self-consistent model of the Jovian auroral thermal structure, *J. Geophys. Res.*, *106*(A7), 12,933–12,952, doi:10.1029/2000JA900129.

Grodent, D., J. T. Clarke, J. H. Waite Jr., S. W. H. Cowley, J.-C. Gérard, and J. Kim (2003), Jupiter's polar auroral emissions, *J. Geophys. Res.*, *108*(A10), 1366, doi:10.1029/2003JA010017.

Gustin, J., J.-C. Gérard, D. Grodent, S. W. H. Cowley, J. T. Clarke, and A. Grard (2004a), Energy-flux relationship in the FUV Jovian aurora deduced from HST-STIS spectral observations, *J. Geophys. Res.*, *109*, A10205, doi:10.1029/2003JA010365.

Gustin, J., et al. (2004b), Jovian auroral spectroscopy with FUSE: Analysis of self-absorption and implications for electron precipitation, *Icarus*, *171*, 336–355, doi:10.1016/j.icarus.2004.06.005.

Gustin, J., J.-C. Gérard, G. R. Gladstone, D. Grodent, and J. T. Clarke (2006), Characteristics of Jovian morning bright FUV aurora from Hubble Space telescope imaging spectrograph imaging spectral observations, *J. Geophys. Res.*, *111*, A09220, doi:10.1029/2006JA011730.

Gustin, J., B. Bonfond, D. Grodent, and J.-C. Gérard (2012), Conversion from HST ACS and STIS auroral counts into brightness, precipitated power, and radiated power for H_2 giant planets, *J. Geophys. Res.*, *117*, A07316, doi:10.1029/2012JA017607.

Harris, W., J. T. Clarke, M. A. McGrath, and G. E. Ballester (1996), Analysis of Jovian auroral H Ly-α emission (1981–1991), *Icarus*, *123*, 350–365, doi:10.1006/icar.1996.0164.

Hess, S. L. G., B. Bonfond, P. Zarka, and D. Grodent (2011), Model of the Jovian magnetic field topology constrained by the Io auroral emissions, *J. Geophys. Res.*, *116*, A05217, doi:10.1029/2010JA016262.

Hess, S. L. G., et al. (2013), Evolution of the Io footprint brightness II: Modeling, *Planet. Space Sci.*, *88*, 76–85, doi:10.1016/j.pss.2013.08.005.

Hill, T. W. (2001), The Jovian auroral oval, *J. Geophys. Res.*, *106*(A5), 8101–8107, doi:10.1029/2000JA000302.

Jones, S. T., and Y.-J. Su (2008), Role of dispersive Alfvén waves in generating parallel electric fields along the Io-Jupiter fluxtube, *J. Geophys. Res.*, *113*, A12205, doi:10.1029/2008JA013512.

Kim, Y. H., J. L. Fox, and J. J. Caldwell (1997), Temperatures and altitudes of Jupiter's ultraviolet aurora inferred from GHRS Observations with the Hubble Space Telescope, *Icarus*, *128*, 189–201, doi:10.1006/icar.1997.5699.

Kimble, R. A., et al. (1998), The on-orbit performance of the space telescope imaging spectrograph, *Astrophys. J. Lett.*, *492*, L83, doi:10.1086/311102.

Knight, S. (1973), Parallel electric fields, *Planet. Space Sci.*, *21*, 741–750, doi:10.1016/0032-0633(73)90093-7.

Lam, H. A., N. Achilleos, S. Miller, J. Tennyson, L. M. Trafton, T. R. Geballe, and G. E. Ballester (1997), A baseline spectroscopic study of the in-frared auroras of Jupiter, *Icarus*, *127*, 379–393, doi:10.1006/icar.1997.5698.

Livengood, T. A., D. F. Strobel, and H. W. Moos (1990), Long-term study of longitudinal dependence in primary particle precipitation in the north Jovian aurora, *J. Geophys. Res.*, *95*(A7), 10,375–10,388, doi:10.1029/JA095iA07p10375.

Mauk, B. H., J. T. Clarke, D. Grodent, J. H. Waite Jr., C. P. Paranicas, and D. J. Williams (2002a), Transient aurora on Jupiter from injections of magnetospheric electrons, *Nature*, *415*, 1003–1005, doi:10.1038/4151003a.

Mauk, B. H., B. J. Anderson, and R. M. Thorne (2002b), Magnetosphere-ionosphere coupling at Earth, Jupiter and beyond, in *Atmosphere in the Solar System: Comparative Aeronomy*, edited by M. Mendillo, A. Nagy, and J. H. Waite, AGU, Washington, D. C.

Morrissey, P. F., P. D. Feldman, J. T. Clarke, B. C. Wolven, D. F. Strobel, S. T. Durrance, and J. T. Trauger (1997), Simultaneous spectroscopy and imaging of the Jovian aurora with the Hopkins Ultraviolet Telescope and the Hubble Space Telescope, *Astrophys. J.*, *476*, 918, doi:10.1086/303648.

Moses, J. I., T. Fouchet, B. Bézard, G. R. Gladstone, E. Lellouch, and H. Feuchtgruber (2005), Photochemistry and diffusion in Jupiter's stratosphere: Constraints from ISO observations and comparisons with other giant planets, *J. Geophys. Res.*, *110*, E08001, doi:10.1029/2005JE002411.

Nichols, J. D., J. T. Clarke, J. C. Gérard, D. Grodent, and K. C. Hansen (2009), Variation of different components of Jupiter's auroral emission, *J. Geophys. Res.*, *114*, A06210, doi:10.1029/2009JA014051.

Nichols, J., and S. W. H. Cowley (2004), Magnetosphere-ionosphere coupling currents in Jupiter's middle magnetosphere: Effect of precipita-tion induced enhancement of the ionospheric Pedersen conductivity, *Ann. Geophys.*, *22*, 1799–1827, doi:10.5194/angeo-22-1799-2004.

Ozak, N., T. E. Cravens, and D. R. Schultz (2013), Auroral ion precipitation at Jupiter: Predictions for Juno, *Geophys. Res. Lett.*, *40*, 4144–4148, doi:10.1002/grl.50812.

Parkinson, C. D., A. I. F. Stewart, A. S. Wong, Y. L. Yung, and J. M. Ajello (2006), Enhanced transport in the polar mesosphere of Jupiter: Evidence from Cassini UVIS helium 584 Å airglow, *J. Geophys. Res.*, *111*, E02002, doi:10.1029/2005JE002539.

Radioti, A., A. T. Tomás, D. Grodent, J.-C. Gérard, J. Gustin, B. Bonfond, N. Krupp, J. Woch, and J. D. Menietti (2009), Equatorward diffuse auroral emissions at Jupiter: Simultaneous HST and Galileo observations, *Geophys. Res. Lett.*, *36*, L07101, doi:10.1029/2009GL037857.

Ray, L. C., R. E. Ergun, P. A. Delamere, and F. Bagenal (2010), Magnetosphere-ionosphere coupling at Jupiter: Effect of field-aligned potentials on angular momentum transport, *J. Geophys. Res.*, *115*, A09211, doi:10.1029/2010JA015423.

Ray, L. C., R. E. Ergun, P. A. Delamere, and F. Bagenal (2012), Magnetosphere-ionosphere coupling at Jupiter: A parameter space study, *J. Geophys. Res.*, *117*, A01205, doi:10.1029/2011JA016899.

Trafton, L., J.-C. Gérard, G. Munhoven, and J. H. Waite Jr. (1994), High-resolution spectra of Jupiter's northern auroral ultraviolet emission with the Hubble Space Telescope, *Astrophys. J.*, *421*, 816–827, doi:10.1086/173694.

Waite, J. H., Jr., et al. (2001), An auroral flare at Jupiter, *Nature*, *410*, 787–789.

Wolven, B. C., and P. D. Feldman (1998), Self-absorption by vibrationally excited H2 in the Astro-2 Hopkins ultraviolet telescope spectrum of the Jovian aurora, *Geophys. Res. Lett.*, *25*, 1537–1540, doi:10.1029/98GL01063.

Yung, Y. L., G. R. Gladstone, K. M. Chang, J. M. Ajello, and S. K. Srivastava (1982), H2 fluorescence spectrum from 1200 to 1700 Å by electron impact: Laboratory study and application to Jovian aurora, *Astrophys. J.*, *254*, L65–L69, doi:10.1086/183757.